Forward volume magnetoacoustic spin wave excitation with micron-scale spatial resolution

M. Küß, F. Porrati, Andreas Hörner, M. Weiler, Manfred Albrecht, M. Huth, Achim Wixforth

Angaben zur Veröffentlichung / Publication details:

Küß, M., F. Porrati, Andreas Hörner, M. Weiler, Manfred Albrecht, M. Huth, and Achim Wixforth. 2022. "Forward volume magnetoacoustic spin wave excitation with micron-scale spatial resolution." *APL Materials* 10 (8): 081112. https://doi.org/10.1063/5.0101526.

APL Materials

Forward volume magnetoacoustic spin wave excitation with micron-scale spatial resolution

Cite as: APL Mater. **10**, 081112 (2022); https://doi.org/10.1063/5.0101526
Submitted: 01 June 2022 • Accepted: 04 July 2022 • Published Online: 29 August 2022

M. Küß, F. Porrati, A. Hörner, et al.

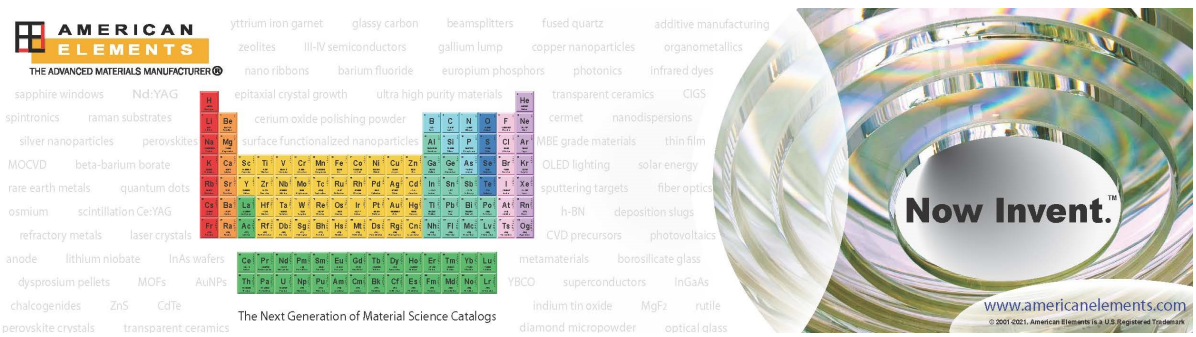

Forward volume magnetoacoustic spin wave excitation with micron-scale spatial resolution

Cite as: APL Mater. 10, 081112 (2022); doi: 10.1063/5.0101526
Submitted: 1 June 2022 • Accepted: 4 July 2022 •
Published Online: 29 August 2022

M. Küß,[1,a)] F. Porrati,[2] A. Hörner,[1] M. Weiler,[3] M. Albrecht,[4] M. Huth,[2] and A. Wixforth[1]

AFFILIATIONS

[1] Experimental Physics I, Institute of Physics, University of Augsburg, 86135 Augsburg, Germany
[2] Institute of Physics, Goethe University, 60438 Frankfurt am Main, Germany
[3] Fachbereich Physik and Landesforschungszentrum OPTIMAS, Technische Universität Kaiserslautern, 67663 Kaiserslautern, Germany
[4] Experimental Physics IV, Institute of Physics, University of Augsburg, 86135 Augsburg, Germany

Note: This paper is part of the Special Topic on Science and Technology of 3D Magnetic Nanostructures.
[a)] **Author to whom correspondence should be addressed:** matthias.kuess@physik.uni-augsburg.de

ABSTRACT

The interaction between surface acoustic waves (SAWs) and spin waves (SWs) in a piezoelectric-magnetic thin film heterostructure yields potential for the realization of novel microwave devices and applications in magnonics. In the present work, we characterize magnetoacoustic waves in three adjacent magnetic micro-stripes made from CoFe + Ga, CoFe, and CoFe + Pt with a single pair of tapered interdigital transducers (TIDTs). The magnetic micro-stripes were deposited by focused electron beam-induced deposition and focused ion beam-induced deposition direct-writing techniques. The transmission characteristics of the TIDTs are leveraged to selectively address the individual micro-stripes. Here, the external magnetic field is continuously rotated out of the plane of the magnetic thin film and the forward volume SW geometry is probed with the external magnetic field along the film normal. Our experimental findings are well explained by an extended phenomenological model based on a modified Landau–Lifshitz–Gilbert approach that considers SWs with nonzero wave vectors. Magnetoelastic excitation of forward volume SWs is possible because of the vertical shear strain ε_{xz} of the Rayleigh-type SAW.

I. INTRODUCTION

Over the last decade, increasing attention has been paid to the resonant coupling between surface acoustic waves (SAWs) and spin waves (SWs).[1–3] On the one hand, magnetoacoustic interaction opens up the route toward energy-efficient SW excitation and manipulation in the field of magnonics.[4] On the other hand, magnetoacoustic interaction greatly affects the properties of the SAW, which, in turn, can be used to devise new types of microwave devices, such as magnetoacoustic sensors[5,6] or microwave acoustic isolators.[7–14] High flexibility in the design of these devices is possible since the properties of the SWs can be varied in a wide range of parameters. For instance, the SW dispersion can be reprogrammed by external magnetic fields or electrical currents[15,16] and more complex design of the magnet geometry[17,18] or use of multilayers[14,19–21] to allow for multiple dispersion branches with potentially large nonreciprocal behavior. Conversely, the SAW–SW interaction can be also used as an alternative method to characterize magnetic thin films, SWs, and SAWs.[12,20,22,23] Design of future magnetoacoustic devices can benefit from the fact that SAW technology is well developed and already employed in manifold ways in our daily life.[24–27] Efficient excitation and detection of SAWs with metallic comb-shaped electrodes—so-called interdigital transducers (IDTs)—are possible on piezoelectric substrates. For example, acoustic delay lines with low insertion losses of about 6 dB at 4 GHz have been realized.[28] Fundamental limitations in the SAW excitation efficiency are mainly given by interaction with thermal phonons, spurious excitation of longitudinal acoustic waves in the air, and nonlinear effects at high input power.[27,29] So far, IDTs exciting SAWs homogeneously over the whole aperture have been used in resonant magnetoacoustic experiments. Apart from Refs. 30 and 31, these studies have

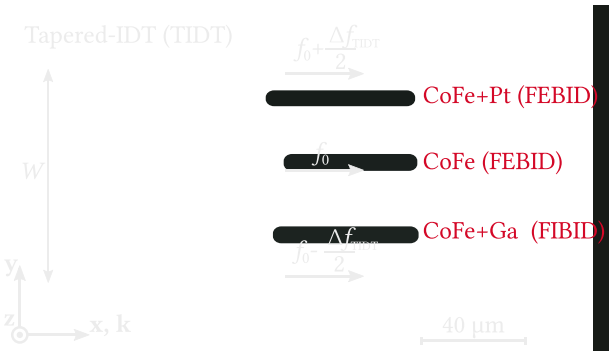

FIG. 1. Optical micrograph of the fabricated device. Rayleigh-type SAWs are excited on the piezoelectric substrate $LiNbO_3$ by a tapered-IDT (TIDT) within a wide range of frequencies $f_0 - \frac{\Delta f_{\mathrm{TIDT}}}{2}, \ldots, f_0 + \frac{\Delta f_{\mathrm{TIDT}}}{2}$. In dependence on the applied frequency, SWs can be magnetoacoustically excited in one of the three different magnetic micro-stripes deposited by FEBID and FIBID. Magnetoacoustic transmission measurements are performed by a pair of TIDTs.

been performed with an external magnetic field that was exclusively oriented in the plane of the magnetic thin film.

Here, we experimentally demonstrate targeted magnetoacoustic excitation and characterization of SWs in the forward volume SW geometry with micrometer-scale spatial resolution. To do so, magnetoacoustic transmission measurements are performed with one pair of tapered interdigital transducers (TIDTs) at three different magnetic micro-stripes, as shown in Fig. 1. This study is carried out in different geometries in which the external magnetic field is tilted out of the plane of the magnetic thin film. We demonstrate that magnetoelastic excitation of SWs is possible even if the static magnetization is parallel to the magnetic film normal—which is the so-called forward volume spin wave (FVSW) geometry—thanks to the vertical shear strain component ε_{xz} of the Rayleigh-type SAW. The experimental results are simulated with an extended phenomenological model, which takes the arbitrary orientation of the external magnetic field and magnetization into account.

The magnetic micro-stripes with lateral dimensions of about $20 \times 40\ \mu\mathrm{m}^2$ and different magnetic properties were deposited by focused electron beam-induced deposition (FEBID) and focused ion beam-induced deposition (FIBID). One particular advantage of using the direct-write approach[32,33] to fabricate the micro-stripes is the ease with which the magnetic properties can be tailored, such as the saturation magnetization.[34] Moreover, direct-write capabilities make the fabrication of complex 3D magnetic structures on the nanoscale possible. Applications in magnonics include, for instance, 3D nanovolcanoes with tunable higher-frequency eigenmodes,[35] 2D and 3D magnonic crystals with SW bandgaps,[36,37] SW beam steering via graded refractive index, and frustrated 3D magnetic lattices.[38,39]

II. THEORY

A surface acoustic wave is a sound wave propagating along the surface of a solid material with evanescent displacement normal to the surface. The density, surface boundary conditions, and elastic, dielectric, and potentially piezoelectric properties of the material mainly determine if and which SAW mode can be launched. Typical SAW modes on homogeneous substrates show a linear dispersion with a constant propagation velocity of about $c_{\mathrm{SAW}} = 3500$ m/s.[27] We use a standard Y-cut Z-propagation $LiNbO_3$ substrate, which gives rise to a Rayleigh-type SAW. On the substrate surface, this SAW mode causes a retrograde elliptical lattice motion in a plane defined by the SAW propagation direction and the surface normal.[27,40]

An optical micrograph of the fabricated magnetoacoustic device is shown in Fig. 1. Rayleigh-type SAWs can be excited in a frequency range between $f_0 - \frac{\Delta f_{\mathrm{TIDT}}}{2}, \ldots, f_0 + \frac{\Delta f_{\mathrm{TIDT}}}{2}$, which corresponds to different positions of the TIDT along the length of its aperture W. To describe the magnetoacoustic transmission of the three different magnetic thin films, we extend the phenomenological model of Dreher *et al.*[30] and Küß *et al.*[12] in terms of magnetoacoustically excited SWs with nonzero wave vector and arbitrary orientation of the equilibrium magnetization direction, as detailed below.

A. Magnetoacoustic driving fields and SAW transmission

In the following, we use the (x, y, z) coordinate system shown in Fig. 2.[30] The x and z axes are parallel to the wave vector $\mathbf{k}_{\mathrm{SAW}} = k\hat{\mathbf{x}}$ of the SAW and normal to the plane of the magnetic micro-stripes, respectively. The equilibrium direction of the magnetization $\mathbf{M}$ and the orientation of the external magnetic field $\mathbf{H}$ are specified by the angles (θ_0, ϕ_0) and (θ_H, ϕ_H). Here, θ_0 and ϕ_0 are calculated by minimization of the static free energy. For that, we take the external magnetic field $\mathbf{H}$, thin film shape anisotropy $M_s\hat{\mathbf{z}}$ with saturation magnetization M_s, and a small uniaxial in-plane anisotropy H_{ani}, which encloses an angle ϕ_{ani} with the x axis, into account.[12,30] Because the characterized magnetic thin films are relatively[12] thick ($d \geq 24$ nm), we neglect the surface anisotropy. The SAW–SW interaction can be described by effective dynamic magnetoacoustic driving fields, which exert a torque on the static magnetization.[41] The resulting damped precession of $\mathbf{M}$ is then determined by the

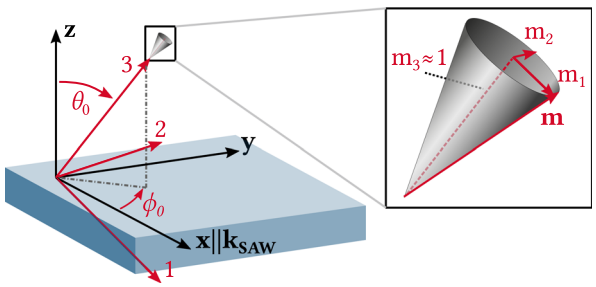

FIG. 2. Relation between the coordinate systems employed. The (x, y, z) frame of reference is defined by the SAW propagation direction and the surface normal. We employ the (1,2,3) coordinate system to solve the LLG equation. Here, the 3-direction corresponds to the equilibrium magnetization orientation and the 2-direction is always aligned in the plane of the magnetic film. The inset shows the precession cone of the magnetization, with the transverse magnetization components m_1 and m_2. The coordinate system is taken from Ref. 30.

Landau–Lifshitz–Gilbert (LLG) equation for small precession amplitudes. To this end, we introduce the rotated $(1,2,3)$ Cartesian coordinate system in Fig. 2. The 3-axis is parallel to **M** and the 2-axis is aligned in the film plane.[41] In this phenomenological model, it is assumed that the frequencies f and wave vectors k of SAW and SW are identical.[12,42] We assume that the magnon–phonon coupling strength is in the weak coupling regime, as discussed for the three micro-stripes in Appendix A. Furthermore, only magnetic films with small thicknesses $|k|d \ll 1$ and homogeneous strain in the z-direction of the magnetic film are considered.[12,30]

The effective magnetoacoustic driving field as a function of SAW power in the (1,2) plane can be written[12] as

$$\mathbf{h}(x,t) = \begin{pmatrix} \tilde{h}_1 \\ \tilde{h}_2 \end{pmatrix} \sqrt{\frac{k}{R\, c_{\mathrm{SAW}} w}} \sqrt{P_{\mathrm{SAW}}(x)}\; \mathrm{e}^{i(kx-\omega t)}. \tag{1}$$

Here, $\omega = 2\pi f$ and c_{SAW} are the angular frequency and propagation velocity of the SAW, w is the width of the acoustic beam, and the constant $R = 1.4 \times 10^{11}$ J/m^3 [43] The normalized effective magnetoelastic driving fields $\tilde{h}_1$ and $\tilde{h}_2$ of a Rayleigh wave with strain components $\varepsilon_{kl=xx,zz,xz} \neq 0$ are[12,30]

$$\begin{pmatrix} \tilde{h}_1 \\ \tilde{h}_2 \end{pmatrix} = \frac{2}{\mu_0}\left[b_1 \tilde{a}_{xx} \begin{pmatrix} -\sin\theta_0 \cos\theta_0 \cos^2\phi_0 \\ \sin\theta_0 \sin\phi_0 \cos\phi_0 \end{pmatrix} + b_1 \tilde{a}_{zz} \begin{pmatrix} \sin\theta_0 \cos\theta_0 \\ 0 \end{pmatrix} + b_2 \tilde{a}_{xz} \begin{pmatrix} -\cos(2\theta_0) \cos\phi_0 \\ \cos\theta_0 \sin\phi_0 \end{pmatrix} \right], \tag{2}$$

where $b_{1,2}$ are the magnetoelastic coupling constants for cubic symmetry of the ferromagnetic layer,[7,30] $\tilde{a}_{kl} = \varepsilon_{kl,0}/(|k||u_{z,0}|)$ are the normalized amplitudes of the strain, and $\varepsilon_{kl,0}$ are the complex amplitudes of the strain. Furthermore, $u_{z,0}$ is the amplitude of the lattice displacement in the z-direction. For the sake of simplicity, we neglect non-magnetoelastic interactions, such as magneto-rotation coupling,[12,22,44] spin-rotation coupling,[45–47] and gyromagnetic coupling.[48] In contrast to previous magnetoacoustic studies[10,12,20,22,23,42,49] where the equilibrium magnetization direction was aligned in the plane of the magnetic film ($\theta_0 = 90°$), the strain component ε_{zz} results in a modified driving field for geometries with $\theta_0 \neq 90°$.

In the experiments, we characterize the SAW–SW interaction for the three geometries depicted in Fig. 3. The oop0-, oop45-, and oop90-geometries are defined by the polar angle ϕ_H of the external magnetic field **H**. Since the symmetry of the magnetoacoustic driving field **h** essentially determines the magnitude of the magnetoacoustic interaction, we will now discuss the orientation dependence of $|\mu_0 \tilde{\mathbf{h}}(\theta_0)|$ for the Rayleigh wave strain components ε_{xx}, ε_{zz}, and ε_{xz} separately, setting all other strain components equal to zero.[30] In Fig. 4, we show a polar plot of the normalized magnitude of the driving field $|\mu_0 \tilde{\mathbf{h}}(\theta_0)|$, using $2b_{1,2}\tilde{a}_{kl} = 1$ T and assuming no in-plane anisotropy ($H_{\mathrm{ani}} = 0, \phi_0 = \phi_H$). First, it is interesting that magnetoelastic excitation of SWs in the FV-geometry ($\theta_0 = 0°$) can be solely mediated by the driving fields of the shear component ε_{xz}.

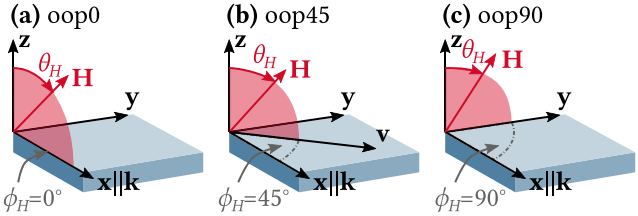

FIG. 3. The magnetoacoustic transmission is studied in the three geometries oop0, oop45, and oop90, which are defined by the polar angle ϕ_H of the external magnetic field **H**. Here, **H** is tilted with respect to the z axis by the azimuthal angle θ_H.

Second, finite element method (FEM) eigenmode simulations reveal[50] that the strain component ε_{zz} is phase shifted by π with respect to ε_{xx}. Thus, the magnetoacoustic driving fields of ε_{xx} and ε_{zz} show a constructive superposition. Third, the SAW–SW helicity mismatch effect arises because of a $\pm\pi/2$ phase shift of ε_{xz} with respect to ε_{xx}.[8–12,23,30] Under an inversion of the SAW propagation direction ($k \to -k$, or $k_{S21} \to k_{S12}$), the phase shift changes its sign ($\pi/2 \to -\pi/2$). For measurements in the in-plane geometry, the SAW–SW helicity mismatch effect is attributed to a superposition of driving fields caused by ε_{xx} and ε_{xz}. This is in contrast to the oop90-geometry ($\phi_0 = 90°$), where the SAW–SW helicity mismatch effect is mediated by the strain components ε_{zz} and ε_{xz}.

The magnetoacoustic driving field causes the excitation of SWs in the magnetic film. Thus, the power of the traveling SAW is exponentially decaying while propagating through the magnetic film with

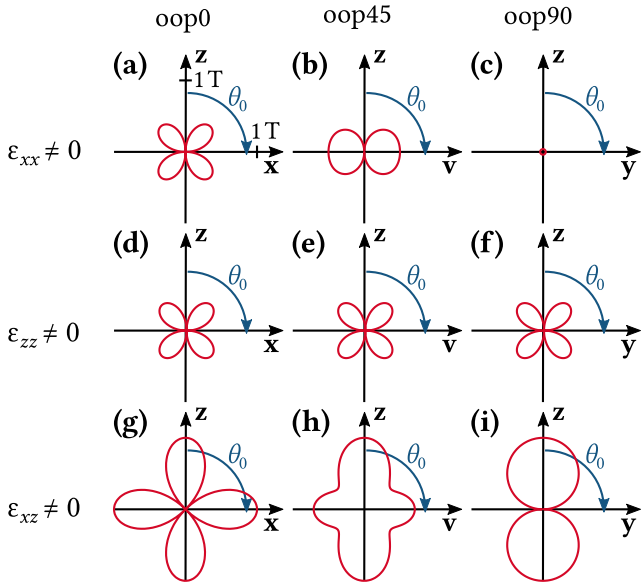

FIG. 4. Polar plot of the normalized driving field's magnitude $|\mu_0 \tilde{\mathbf{h}}(\theta_0)|$ for the relevant strain components ε_{xx}, ε_{zz}, and ε_{xz} and for the different geometries oop0, oop45, and oop90, assuming $\phi_0 = \phi_H$. The distance from the origin indicates for all panels the normalized magnitude of the driving field. Thereby, the driving field was calculated by using Eq. (2) with $2b_{1,2}\tilde{a}_{kl} = 1$ T. This diagram extends Fig. 4 of Ref. 30 by panels (c)–(f) and (i).

length l_f and thickness d. With respect to the initial power P_0, the absorbed power of the SAW is

$$P_{\text{abs}} = P_0\left(1 - \exp\left\{-C\ \text{Im}\left[(\tilde{\mathbf{h}})^*\tilde{\chi}\tilde{\mathbf{h}}\right]\right\}\right) \text{ with } C = \frac{1}{2}\mu_0 l_f d\left(\frac{k^2}{R}\right). \quad (3)$$

The magnetic susceptibility tensor $\tilde{\chi}$ describes the magnetic response to small time-varying magnetoacoustic fields and is calculated as described by Dreher *et al.*[30] for arbitrary equilibrium magnetization directions (θ_0, ϕ_0). Besides the external magnetic field, exchange coupling, and uniaxial in-plane anisotropy, we take the dipolar fields for SWs with $k \neq 0$ also into account, which are given in Eq. (B1) in Appendix B.

Finally, to directly simulate the experimentally determined relative change of the SAW transmission ΔS_{ij} on the logarithmic scale, we use

$$\Delta S_{ij} = 10\ \text{lg}\left(\frac{P_0 - P_{\text{abs}}}{P_0}\right) \text{ with } ij = \begin{cases} 21 & \text{for } k \geq 0, \\ 12 & \text{for } k < 0, \end{cases} \quad (4)$$

for SAWs propagating parallel $(k \geq 0)$ and antiparallel $(k < 0)$ to the x axis.

B. Spin wave dispersion

Resonant SAW–SW excitation is possible if the dispersion relations of SAW and SW intersect in the uncoupled state. The SW dispersion is obtained by setting $\det(\tilde{\chi}^{-1}) = 0$ and taking the real part of the solution for small SW damping constants α. If we neglect the uniaxial in-plane anisotropy ($H_{\text{ani}} = 0$, $\phi_0 = \phi_H$), we obtain[51]

$$f = \frac{\gamma\mu_0}{2\pi}\sqrt{H_{11}H_{22} - H_{12}^2}, \quad (5)$$

with

$$\begin{aligned} H_{11} &= H\cos(\theta_0 - \theta_H) + Dk^2 - M_s\cos(2\theta_0) \\ &\quad + M_s(1 - G_0)\left(\cos(2\theta_0) - \sin^2\phi_0\cos^2\theta_0\right), \\ H_{22} &= H\cos(\theta_0 - \theta_H) + Dk^2 - M_s\cos^2\theta_0 + M_s(1 - G_0)\sin^2\phi_0, \\ H_{12} &= M_s(1 - G_0)\sin\phi_0\cos\phi_0\cos\theta_0. \end{aligned} \quad (6)$$

Here, γ is the gyromagnetic ratio, $G_0 = \frac{1-e^{-|k|d}}{|k|d}$ and $D = \frac{2A}{\mu_0 M_s}$ with the magnetic exchange constant A.

We exemplarily calculated the SW resonance frequency f in Fig. 5(a) for the oop0-geometry as a function of the external magnetic field magnitude $\mu_0 H$. The corresponding azimuthal angle θ_0 of the equilibrium magnetization orientation is shown in Fig. 5(b). For the simulation, we use besides $\phi_0 = 0°$, $k = 5.9\ \mu\text{m}^{-1}$, $\mu_0 M_s = 1$ T, and $H_{\text{ani}} = 0$ the parameters of the CoFe + Ga thin film in Table II. Additionally, the resonance frequency $f = 3$ GHz of a SAW with $k = 5.9\ \mu\text{m}^{-1}$ is depicted by the dashed line in Fig. 5(a). The dispersion $f(\mu_0 H)$ changes strongly with the azimuthal angle θ_H of the applied external magnetic field. For the FVSW geometry $\theta_H = 0°$, the magnetic thin film is saturated ($\theta_0 = 0°$) when the magnetic field overcomes the magnetic shape anisotropy $\mu_0 H > \mu_0 M_s$ and resonant

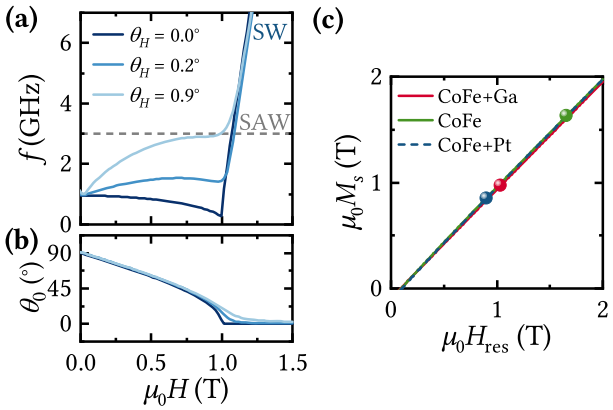

FIG. 5. (a) The SW resonance frequency f is calculated with Eq. (5) for the oop0-geometry as a function of the external magnetic field magnitude $\mu_0 H$ and azimuthal angle θ_H. The corresponding azimuthal angle θ_0 of the equilibrium magnetization orientation is shown in (b). For the simulation, we use $\phi_0 = 0°$, $k = 5.9\ \mu\text{m}^{-1}$, $\mu_0 M_s = 1$ T, and zero in-plane anisotropy. The remaining parameters are taken from the data for CoFe + Ga thin film in Table II. (c) The saturation magnetizations M_s of the three different magnetic thin films (colored dots) are calculated from the experimentally determined resonance field $\mu_0 H_{\text{res}}$ of the FVSW in Fig. 8. The general dependence $\mu_0 M_s(\mu_0 H_{\text{res}})$ is shown by the lines for the different magnetic films.

SAW–SW interaction is only possible at $\mu_0 H = 1.06$ T. In contrast, for $\theta_H = 0.9°$, we expect magnetoacoustic interaction in a wide range $\mu_0 H \approx 0.7, \ldots, 1.0$ T, where the dispersions of SAW and SW intersect. For this geometry and $\mu_0 H \leq 1.5$ T, the magnetic film is not fully saturated ($\theta_0 \neq 0.9°$).

III. EXPERIMENTAL SETUP

In contrast to previous magnetoacoustic studies performed with conventional IDTs,[10,12,20,22,23,31,42,49] here, we use "tapered" or "slanted" interdigital transducers (TIDTs)[52–55] to characterize SAW–SW interaction in three different magnetic thin micro-stripes in one run. Although the fingers of the TIDT are slanted, the SAW propagates dominantly parallel to the x axis in Fig. 1 because of the strong beam steering effect of the Y-cut Z-propagation $LiNbO_3$ substrate.[27,52] The linear change of the periodicity $p(y)$ along the transducer aperture W results in a spatial dependence of the SAW resonance frequency $f(y) = c_{\text{SAW}}/p(y)$.[52] Thus, a TIDT has a wide transmission band and can be thought of as consisting of multiple conventional IDTs that are connected electrically in parallel.[54] In good approximation, the frequency bandwidth of a conventional IDT is given by $\Delta f_{\text{IDT}} = 0.9 f_0/N$ and is constant for higher harmonic resonance frequencies. From the bandwidth Δf_{TIDT} of the TIDT, the width of the acoustic beam w at constant frequency can be estimated[55] with

$$w = W\frac{\Delta f_{\text{IDT}}}{\Delta f_{\text{TIDT}}}. \quad (7)$$

The TIDTs are fabricated out of Ti(5)/Al(70) (all thicknesses are given in units of nm) and have an aperture of $W = 100\ \mu$m, the number of finger-pairs is $N = 22$, and the periodicity $p(y)$ changes from 3.08 to 3.72 μm. As shown in Fig. 6(a), we operate the TIDT

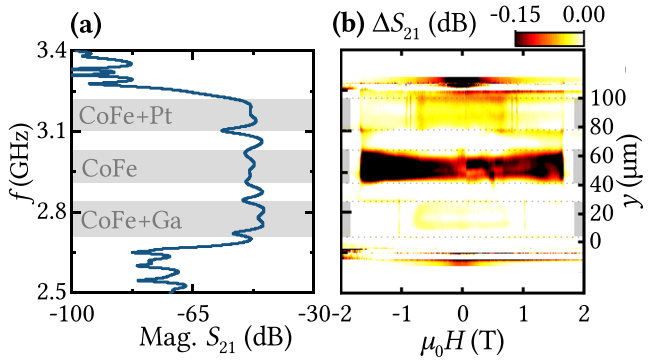

FIG. 6. (a) The transmission characteristics of the fabricated device shows the expected wide band behavior. (b) Within this transmission band, the magnetoacoustic transmission $\Delta S_{21}(\mu_0 H)$ differs for the three different frequency sub-bands that correspond to the three different magnetic films.

at the third harmonic resonance, which corresponds to a transmission band and SAW wavelength in the ranges of 2.69 GHz < f < 3.22 GHz and 1.06 μm < λ < 1.27 μm. According to Eq. (7), we expect for the width of the acoustic beam at constant frequency w = 100 μm (41/530 MHz) ≈ 7.7 μm. Moreover, Streibel *et al.* argue that internal acoustic reflections in the single electrode structure used additionally lowers w by a factor of about four.[55] Since λ is in the range of w, diffraction effects can be expected. These beam spreading losses are partly compensated by the beam steering effect and the frequency selectivity of the receiving transducer, which filters out the diffracted portions of the SAW.[55]

The three different magnetic micro-stripes in Fig. 1 were deposited by direct-writing techniques between the two 800 μm distant TIDTs. For details, we refer the readers to Appendix C. The compositions of the deposited magnetic films were characterized by energy-dispersive x-ray spectroscopy (EDX). The results are summarized in Table I. More details about the microstructure and magnetic properties of CoFe can be found in Refs. 34 and 56. For the microstructure of mixed CoFe–Pt deposits, we refer the readers to Ref. 57 in which results of a detailed investigation of the microstructural and magnetic properties of fully analogous Co–Pt deposits are presented. We determined the thicknesses d and the root mean square roughness of the samples CoFe + Ga (24 ± 2), CoFe (72 ± 2), and CoFe + Pt (70 ± 2) by atomic force microscopy (AFM). The length and widths of all micro-stripes are identical, with l_f = 40 μm and w_f = 20 μm, except $w_f^{\mathrm{CoFe+Ga}}$ = 26 μm.

TABLE I. Compositional EDX analysis of test samples with size 1.5 × 1.5 μm^2. The electron beam voltage was 5 keV for the FEBID samples and 3 keV for the FIBID sample.

Sample	C	O	Fe	Co	Ga	Pt
CoFe + Pt	61.8	6.5	4.2	20.1		7.4
CoFe	26.2	6.9	12.4	54.5		
CoFe + Ga	16.9	16.5	7.7	37.5	21.4	

The SAW transmission of our delay line device was characterized by a vector network analyzer. Based on the low propagation velocity of the SAW, a time-domain gating technique was employed to exclude spurious signals,[58] in particular electromagnetic crosstalk. We use the relative change of the background-corrected SAW transmission signal as

$$\Delta S_{ij}(\mu_0 H) = S_{ij}(\mu_0 H) - S_{ij}(2\,\mathrm{T}) \tag{8}$$

to characterize SAW–SW coupling. Here, ΔS_{ij} is the magnitude of the complex transmission signal with $ij \in \{21, 12\}$. In all measurements, the magnetic field is swept from −2 to 2 T.

IV. DISCUSSION

A. Experimental results

In Fig. 6(b), we show the magnetoacoustic transmission ΔS_{21} as a function of external magnetic field magnitude and frequency for the FVSW geometry ($\theta_H \approx 0°$). Within the wide transmission band of the TIDT, the magnetoacoustic transmission $\Delta S_{21}(\mu_0 H)$ clearly differs for the three different frequency sub-bands, each of which spatially addresses one of the three different magnetic micro-stripes. Both, the maximum change of the transmission with $\mathrm{Max}(\Delta S_{21}^{\mathrm{CoFe}}) > \mathrm{Max}(\Delta S_{21}^{\mathrm{CoFe+Pt}}) > \mathrm{Max}(\Delta S_{21}^{\mathrm{CoFe+Ga}})$ and the resonance fields are different for the three films. The small signals $\Delta S_{21} \neq 0$ at frequencies corresponding to the gaps between the magnetic structures are attributed to diffraction effects. The apparent signal ΔS_{21} at the edges of the transmission band is attributed to measurement noise. From Fig. 6(b), we identify the frequencies corresponding to the centers of the three magnetic films CoFe + Ga, CoFe, and CoFe + Pt as 2.78, 2.96, and 3.17 GHz, respectively. Further analysis is performed at these fixed frequencies.

In Fig. 7, we show the magnetoacoustic transmission $\Delta S_{21}(\mu_0 H, \theta_H)$ of all three films in the oop0-, oop45-, and oop90-geometry (see Fig. 3) as a function of external magnetic field magnitude $\mu_0 H$ and orientation θ_H in the range of $-90° \leq \theta_H \leq 90°$ with an increment of $\Delta\theta_H = 3.6°$. For almost all geometries, the magnetoacoustic response $\Delta S_{21}(\mu_0 H, \theta_H)$ has a star shape symmetry, which was already observed by Dreher *et al.* for Ni(50) thin films.[30] This symmetry results from magnetic shape anisotropy. The sharp resonances in Fig. 7 around $\theta_H = 0°$ are studied in Fig. 8 in the range of $-3.6° \leq \theta_H \leq 3.6°$ with $\Delta\theta_H = 0.225°$ in more detail. For all three magnetic micro-stripes, SWs can be magnetoacoustically excited in the FVSW geometry ($\theta_H = 0°$) and the resonance fields $\mu_0 H_{\mathrm{res}}(\theta_H = 0°)$ differ. Additionally, the symmetry of the magnetoacoustic resonances $\mu_0 H_{\mathrm{res}}(\theta_H)$ changes for the geometries oop0, oop45, and oop90 and the different magnetic micro-stripes. In general, the resonance fields $|\mu_0 H_{\mathrm{res}}|$ decrease if $|\phi_H|$ is increased from 0° to 90° (oop0–oop90). Moreover, the line symmetry with respect to $\theta_H = 0°$ is broken, in particular, for the oop45- and oop90-geometry.

B. Simulation and interpretation

To simulate the experimental results in Figs. 7 and 8 with Eq. (4), we first have to determine the saturation magnetizations M_s of the different magnetic thin films. For this purpose, we compute Eq. (5) for the FVSW geometry ($\theta_H = 0°$, $\theta_0 = 0°$). The relation $M_s(H \equiv H_{\mathrm{res}})$ is shown in Fig. 5(c) for all three magnetic films.

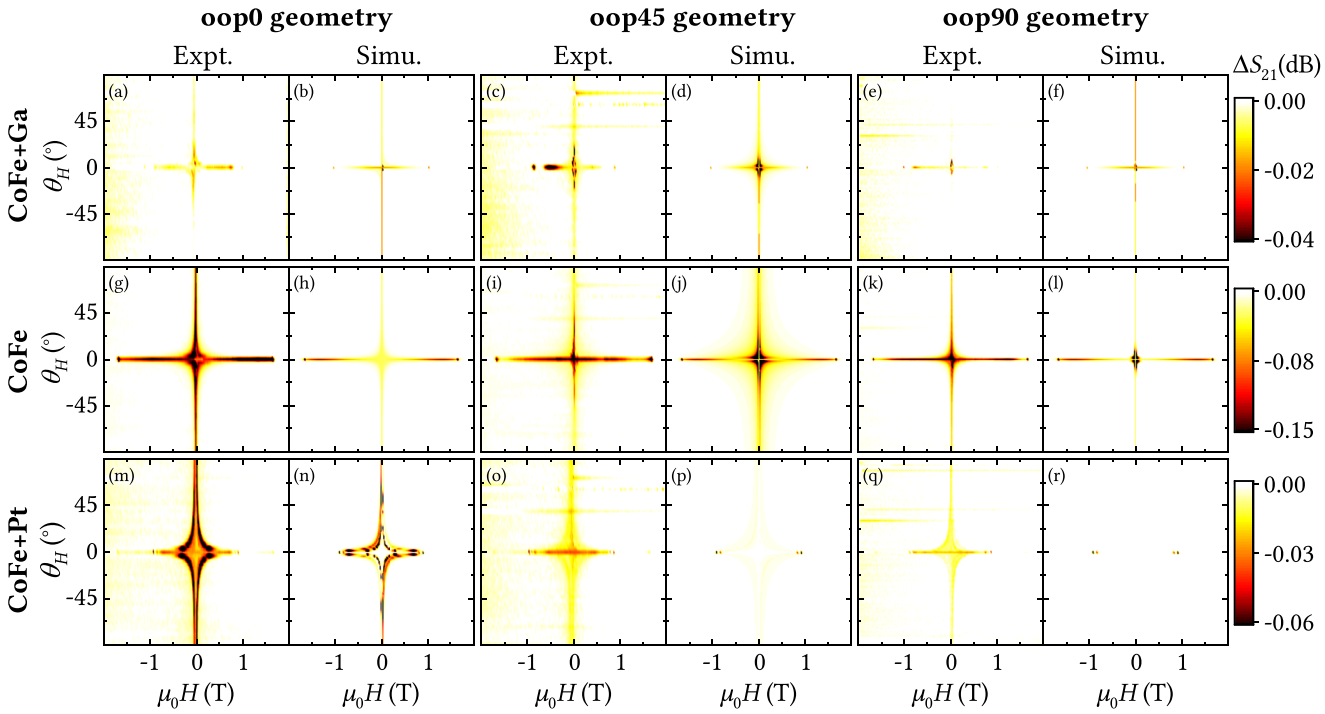

FIG. 7. The magnetoacoustic transmission $\Delta S_{21}(\mu_0 H, \theta_H)$ of the magnetic micro-stripes CoFe + Ga (2.78 GHz), CoFe (2.96 GHz), and CoFe + Pt (3.17 GHz) is shown in the oop0-, oop45-, and oop90-geometry (see Fig. 3). Resonances are observed for $\theta_H = 0°$, which are studied in more detail in Fig. 8. Simulation and experiment show good qualitative agreement.

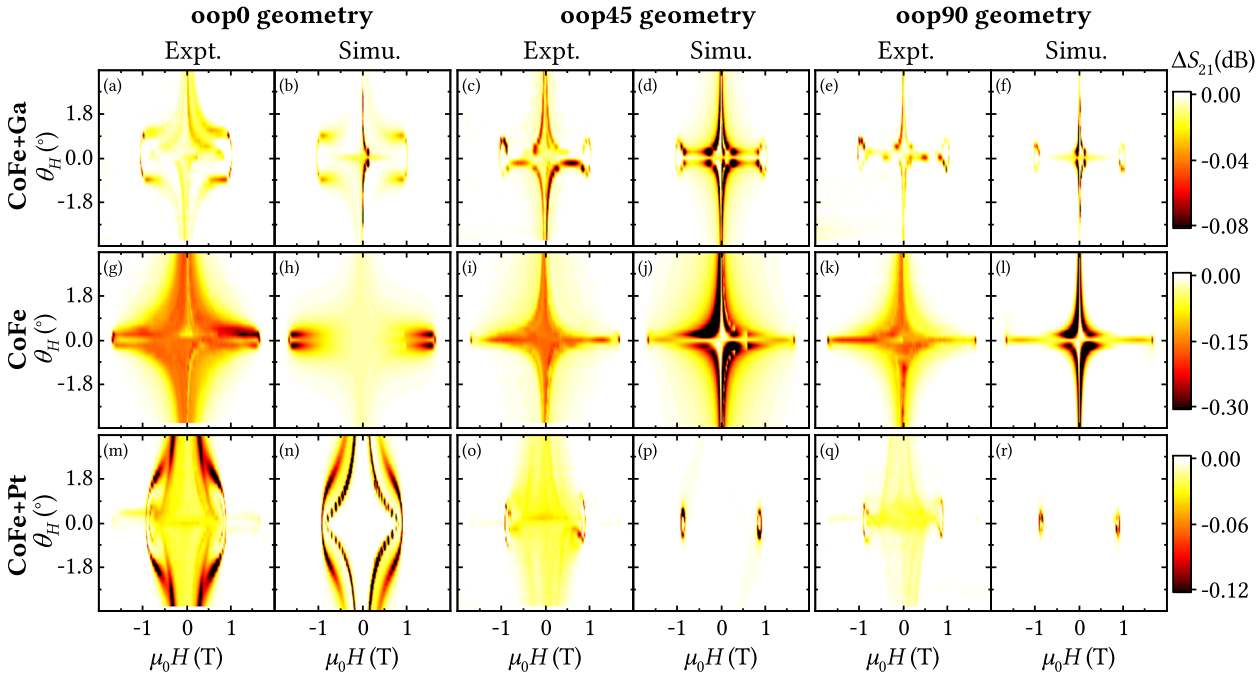

FIG. 8. The magnetoacoustic transmission $\Delta S_{21}(\mu_0 H, \theta_H)$ of the magnetic micro-stripes CoFe + Ga (2.78 GHz), CoFe (2.96 GHz), and CoFe + Pt (3.17 GHz) is shown in the oop0-, oop45-, and oop90-geometry (see Fig. 3) for almost out-of-plane oriented external magnetic field ($\theta_H = -3.6°, \vdots, 3.6°$). Simulation and experiment show good qualitative agreement.

TABLE II. Parameters to simulate the magnetoacoustic transmission ΔS_{21} ($k > 0$) of the Rayleigh-type SAW in Figs. 7–9. For the simulation of ΔS_{12} ($k < 0$), the sign of the normalized strain $\tilde{a}_{xz}$ is inverted. For all micro-stripes, we assume $g = 2.18$[34] and $D = 24.7 \times 10^{-12}$ A m.[34]

	CoFe + Ga	CoFe	CoFe + Pt
d (nm)	24	72	70
f (GHz)	2.78	2.96	3.17
M_s (kA/m)	772	1296	677
α	0.04	0.1	0.05
ϕ_{ani} (deg)	−10	0	88
$\mu_0 H_{\text{ani}}$ (mT)	1	5	10
$\tilde{a}_{xx}$	0.49	0.40	0.40
$\tilde{a}_{zz}$	−0.15	−0.10	−0.10
$\tilde{a}_{xz}$	$0.13i$	$0.17i$	$0.17i$
$\lvert b_1 \rvert$ (T)	4	15	6

Thereby, the frequency f and wave vector k of the SW are determined by the SAW and we assume $c_{\text{SAW}} = 3200$ m/s,[59] $g = 2.18$,[34] and $D = 24.7 \times 10^{-12}$ A m.[34] Since the in-plane anisotropy H_{ani} is expected to be small compared to the shape anisotropy, the impact on the resonance in the FVSW geometry is small, and we use $H_{\text{ani}} = 0$. Under these assumptions, the relations $M_s(H_{\text{res}})$ are almost identical for the three magnetic films. Together with the experimentally determined $\mu_0 H_{\text{res}}(\theta_H = 0^\circ)$ in Fig. 8, the saturation magnetizations of CoFe + Ga, CoFe, and CoFe + Pt are determined to be 772, 1296, and 677 kA/m, respectively.

For the simulations in Figs. 7 and 8, we use the parameters summarized in Table II. The complex amplitudes of the normalized strain $\tilde{a}_{kl} = \varepsilon_{kl,0}/(|k\|u_{z,0}|)$ are estimated from a COMSOL[50] finite element method (FEM) simulation. Since we do not know the elastic constants and density of the magnetic micro-stripes, we assume a pure $LiNbO_3$ substrate with a perfectly conducting overlayer of zero thickness. Thus, the real values of $\tilde{a}_{kl}$ might deviate from the assumed ones.[12] Furthermore, the normalized strain of the simulation was averaged over the thickness $0 \le z \le -d$. The values for the SW effective damping α, magnetoelastic coupling for polycrystalline films[30] $b_1 = b_2$, and small phenomenological uniaxial in-plane anisotropy (H_{ani}, ϕ_{ani}) were adjusted to obtain a good agreement between experiment and simulation. Thereby, α includes Gilbert damping and inhomogeneous line broadening.[12] The phenomenological uniaxial in-plane anisotropy could be caused by substrate clamping effects or the patterning strategy of the FEBID/FIBID direct-write process. Note that the values of all these parameters listed in Table II are very reasonable.

For all three magnetic micro-stripes, the qualitative agreement between simulation and experiment in Figs. 7 and 8 is good. For magnetoelastic interaction, SWs can be excited in the FVSW geometry ($\theta_H = 0^\circ$) solely due to the vertical shear strain ε_{xz}, which causes a nonzero magnetoacoustic driving field, as discussed in Fig. 4. According to Eq. (2), the driving field mediated by $\varepsilon_{xx,zz}$ contributes to $\theta_H \neq 0^\circ$. In Fig. 8, the intensity of the resonances for $\theta_H \neq 0^\circ$ is, therefore, more pronounced than for $\theta_H = 0^\circ$. Because the driving fields, which are mediated by the strain ε_{xx} and ε_{zz}, are in phase, SW excitation in one of the out-of-plane geometries can be even more efficient than in the in-plane geometry. The magnetoacoustic resonance fields of the three magnetic micro-stripes mainly differ due to differences in M_s and d, which strongly affect the corresponding dipolar fields of a SW. As expected from the SW dispersion in Fig. 5(a), we observe in the case of the CoFe + Ga film in Figs. 8(a) and 8(b) for $\theta_H = 0$ a resonance at $\mu_0 H = 1.06$ T with a narrow linewidth and for $\theta_H = 0.9^\circ$ a wide resonance between $\mu_0 H \approx 0.7, \ldots, 1.0$ T. The symmetry of the magnetoacoustic resonances $\mu_0 H_{\text{res}}(\theta_H)$ changes with the geometries oop0, oop45, and oop90 since the magnetic dipolar fields of the SW dispersion Eq. (5) depend on ϕ_0. For CoFe + Pt, two resonances are observed in the oop00-geometry, whereas in the oop45- and oop90-geometry, confined oval-shaped resonances show up. This behavior can be modeled by assuming an uniaxial in-plane anisotropy with $\phi_{\text{ani}} \approx 90^\circ$. In the oop00-geometry, the resonance with the lower resonant fields can be attributed to the switching of the in-plane direction of the equilibrium magnetization direction. In the oop45- and oop90-geometries, the resonance frequencies of the SWs are higher than the excitation frequency of the SAW for $|\theta_H| > 0.7^\circ$. Thus, the magnetoacoustic response ΔS_{21} is low for $|\theta_H| > 0.7^\circ$ in Figs. 8(o)–8(r).

We attribute discrepancies between experiment and simulation to the following effects: The phenomenological model solely considers an in-plane uniaxial anisotropy. Additional in-plane and out-of-plane anisotropies would result in a shift in the resonance fields. Furthermore, the strain is estimated by a simplified FEM simulation and assumed to be homogeneous along the thickness of the micro-stripe. Moreover, we neglect magneto-rotation coupling,[12,22,44] spin-rotation coupling,[45–47] and gyromagnetic coupling.[48] These assumptions have an impact on the intensity and symmetry of the resonances. Finally, low-intensity spurious signals are caused by SAW diffraction effects, which are, for instance, observed in Figs. 8(m), 8(o), and 8(q) for $|\mu_0 H| > 1$ T.

C. Nonreciprocal behavior

The nonreciprocal behavior of the magnetoacoustic wave in the oop0-, oop45-, and oop90-geometries is illustrated for CoFe + Ga in Fig. 9. If the magnetoacoustic wave propagates in inverted directions k_{S21} and k_{S12} (k and $-k$), the magnetoacoustic transmission $\Delta S_{21}(\mu_0 H, \theta_H)$ and $\Delta S_{12}(\mu_0 H, \theta_H)$ differs for the oop45- and oop90-geometry. The qualitative agreement between experiment and simulation is also good with respect to nonreciprocity. The SAW–SW helicity mismatch effect, discussed in the theory section, causes $\Delta S_{21}(\mu_0 H, \theta_H) \neq \Delta S_{12}(\mu_0 H, \theta_H)$ in Fig. 9 and the broken line symmetry with respect to $\theta_H = 0^\circ$ in Figs. 8 and 9. So far, nonreciprocal magnetoacoustic transmission was only observed in studies where the external magnetic field was aligned in the plane of the magnetic film ($\theta_H = 90^\circ$).[8–12,23,30] The magnetoacoustic driving field in Eq. (2) is linearly polarized along the 1-axis for $\phi_0 = 0$. Thus, no nonreciprocity due to the SAW–SW helicity mismatch effect is observed in the oop0-geometry. In contrast, the driving field has a helicity in the oop45- and oop90-geometry. Since this helicity is inverted under inversion of the propagation direction of the SAW ($\varepsilon_{xz,0} \to -\varepsilon_{xz,0}$), nonreciprocal behavior shows up in the oop45- and oop90-geometry. In comparison to the experimental results, the simulation slightly underestimates the nonreciprocity. This is mainly attributed to magneto-rotation coupling,[12,22,44] which can be modeled by a modulated effective coupling constant $b_{2,\text{eff}}$ and

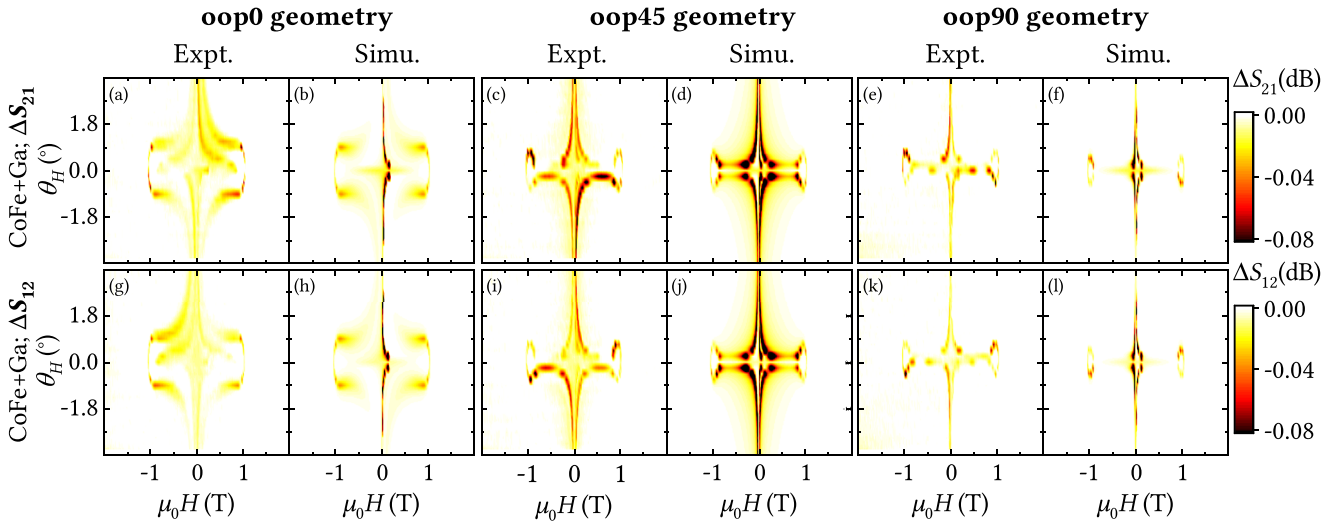

FIG. 9. Nonreciprocal magnetoacoustic waves are characterized by different transmission amplitudes ΔS_{21} and ΔS_{12} for oppositely propagating SAWs with wave vectors k_{S21} and k_{S12}. The nonreciprocal transmission is illustrated for the magnetic micro-stripes CoFe + Ga (2.78 GHz) in the oop0-, oop45-, and oop90-geometry for almost out-of-plane oriented external magnetic field ($\theta_H = -3.6°, \vdots, 3.6°$). Nonreciprocal behavior can solely be observed in the oop45- and oop90-geometry, which is nicely reproduced by the simulation.

can result in an enhancement of the SAW–SW helicity mismatch effect.[12,22]

V. CONCLUSIONS

In conclusion, we have demonstrated magnetoacoustic excitation and characterization of SWs with micrometer-scale spatial resolution using TIDTs. The magnetoacoustic response at different frequencies, which lie within the wide transmission band of the TIDT, can be assigned to the spatially separated CoFe + Ga, CoFe, and CoFe + Pt magnetic micro-stripes. SAW–SW interaction with micrometer-scale spatial resolution can have interesting implications for future applications in magnonics and the realization of new types of microwave devices, such as magnetoacoustic sensors[5,6,60] or microwave acoustic isolators.[14,19–21] For instance, giant nonreciprocal SAW transmission was observed in magnetic bilayers and proposed to build reconfigurable acoustic isolators.[14,19–21] In combination with TIDTs, acoustic isolators, which show in adjacent frequency bands different nonreciprocal behavior, could be realized. Furthermore, if two orthogonal delay lines are combined in a cross-shaped structure, the resolution of magnetoacoustic interaction of different magnetic micro-structures in two dimensions can potentially be achieved.[55,61]

In addition, we extended the theoretical model of magnetoacoustic wave transmission[12,30] in terms of SWs with nonzero wave vector and arbitrary out-of-plane orientation of the static magnetization direction. This phenomenological model provides a good description of the experimental results for CoFe + Ga, CoFe, and CoFe + Pt magnetic micro-stripes in different geometries of the external magnetic field—including the FVSW geometry—in a qualitative way. We find that FVSWs can be magnetoelastically excited by Rayleigh-type SAWs due to the shear strain component ε_{xz}. Moreover, magneto-rotation coupling,[12,22,44] spin-rotation coupling,[45–47] or gyromagnetic coupling[48] may contribute to the excitation of FVSWs. Since the SAW–SW helicity mismatch effect, which is related to ε_{xz} and the effective coupling constant $b_{2,\mathrm{eff}}$, is low in Ni thin films,[9,30,42,62,63] we expect a low excitation efficiency for FVSWs in Ni. In contrast to the previously discussed in-plane geometry, the strain component ε_{zz} of Rayleigh-type waves plays an important role in the out-of-plane geometries and can result in enhanced SAW–SW coupling efficiency and SAW–SW helicity mismatch effect.

ACKNOWLEDGMENTS

This work was funded by the Deutsche Forschungsgemeinschaft (DFG, German Research Foundation)—Project Nos. 391592414 and 492421737. M.H. acknowledges support by the Deutsche Forschungsgemeinschaft (DFG) through the Transregional Collaborative Research Center TRR 288 (Project A04) and through Project No. HU 752/16-1.

AUTHOR DECLARATIONS

Conflict of Interest

The authors have no conflicts to disclose.

Author Contributions

M. Küß: Conceptualization (equal); Data curation (lead); Funding acquisition (equal); Investigation (lead); Validation (lead); Writing – original draft (lead). **F. Porrati:** Formal analysis (equal); Investigation (equal); Methodology (equal); Writing – review & editing (equal). **A. Hörner:** Conceptualization (equal); Funding acquisition

(supporting); Investigation (equal); Methodology (equal); Writing – review & editing (supporting). **M. Weiler:** Supervision (equal); Writing – original draft (equal); Writing – review & editing (equal). **M. Albrecht:** Project administration (equal); Supervision (equal); Writing – review & editing (equal). **M. Huth:** Conceptualization (equal); Investigation (equal); Writing – review & editing (equal). **A. Wixforth:** Conceptualization (lead); Writing – review & editing (equal).

DATA AVAILABILITY

The data that support the findings of this study are available from the corresponding author upon reasonable request.

APPENDIX A: PHONON-MAGNON COUPLING REGIME

Following Ref. 64, we estimate the magnon–phonon coupling strength Ω for all films. To calculate the filling factor from the magnon and phonon overlap, we assume that the SAW extends to within one wavelength λ_{SAW} into the substrate and that the magnon is uniform over the ferromagnetic film thickness. Table III lists the coupling strengths estimated in this way together with the magnon loss rates $\alpha\omega$. For all films, the magnon–phonon coupling is in the weak coupling regime.

APPENDIX B: EFFECTIVE DIPOLAR FIELDS

The effective dipolar fields in the (1,2,3) coordinate system for arbitrary equilibrium magnetization directions (θ_0, ϕ_0) are taken from Ref. 51 by comparing Eq. (23) with the Landau–Lifshitz equation

$$\mathbf{H}^{\mathrm{dip}}_{\mathrm{eff},123} = M_s \begin{pmatrix} H^{\mathrm{dip}}_{11} m_1 + H^{\mathrm{dip}}_{12} m_2 \\ H^{\mathrm{dip}}_{22} m_2 + H^{\mathrm{dip}}_{21} m_1 \\ -\cos^2\theta_0 \end{pmatrix},$$

$$H^{\mathrm{dip}}_{11} = -\cos^2\theta_0 + \cos(2\theta_0) + (1 - G_0)\big(-\cos(2\theta_0) + \sin^2\phi_0 \cos^2\theta_0\big),$$

$$H^{\mathrm{dip}}_{22} = -(1 - G_0)\sin^2\phi_0,$$

$$H^{\mathrm{dip}}_{12} = H^{\mathrm{dip}}_{21} = (1 - G_0)\sin\phi_0 \cos\phi_0 \cos\theta_0. \tag{B1}$$

Here, $m_{1,2}$ are the precession amplitudes of the normalized magnetization $\mathbf{m} = \mathbf{M}/M_s$.

TABLE III. The estimated magnon–phonon coupling strength Ω is for all micro-stripes much smaller than the estimated magnon loss rate $\alpha\omega$.

	CoFe + Ga	CoFe	CoFe + Pt
Ω (MHz)	6	150	60
$\alpha\omega$ (MHz)	700	1900	1000

APPENDIX C: DETAILS ABOUT THE DEPOSITION OF THE MAGNETIC THIN FILMS

FEBID and FIBID are direct-write lithographic techniques used for the fabrication of samples of various dimensions, shapes, and compositions.[33] In FEBID/FIBID, the adsorbed molecules of a precursor gas injected in a SEM/FIB chamber dissociate by means of the interaction with the electron/ion beam forming the sample during the rastering process.[32] In the present work, the samples were fabricated in a dual beam SEM/FIB microscope (FEI, Nova NanoLab 600) equipped with a Schottky electron emitter. FEBID was employed to fabricate the CoFe and CoFe + Pt samples with the following electron beam parameters: 5 kV acceleration voltage, 1.6 nA beam current, 20 nm pitch, and 1 μs dwell time. The number of passes, i.e., the number of rastering cycles, was 1500. FIBID was used to prepare the CoFe + Ga sample with the following ion beam parameters: 30 kV acceleration voltage, 10 pA ion beam current, 12 nm pitch, 200 ns dwell time, and 500 passes. The precursor $HFeCo_3(CO)_{12}$ was employed to fabricate the CoFe and the CoFe + Ga samples,[65] while $HFeCo_3(CO)_{12}$ and $(CH_3)_3CH_3C_5H_4Pt$ were simultaneously used to grow CoFe + Pt.[66] Standard FEI gas-injection-systems (GIS) were used to flow the precursor gases in the SEM via capillaries with 0.5 mm inner diameter. The capillary–substrate surface distance was about 100 and 1000 μm for the $HFeCo_3(CO)_{12}$ and $(CH_3)_3CH_3C_5H_4Pt$ GIS, respectively. The temperature of the precursors were 64 and 44 °C for $HFeCo_3(CO)_{12}$ and $(CH_3)_3CH_3C_5H_4Pt$, respectively. The basis pressure of the SEM was 5×10^7 mbar, which rose up to about 6×10^7 mbar, during CoFe and CoFe + Ga deposition, and to about 2×10^6 mbar, during CoFe + Pt deposition.

REFERENCES

[1] D. A. Bozhko, V. I. Vasyuchka, A. V. Chumak, and A. A. Serga, "Magnon-phonon interactions in magnon spintronics (review article)," Low Temp. Phys. **46**, 383 (2020).

[2] Y. Li, C. Zhao, W. Zhang, A. Hoffmann, and V. Novosad, "Advances in coherent coupling between magnons and acoustic phonons," APL Mater. **9**, 060902 (2021).

[3] W.-G. Yang and H. Schmidt, "Acoustic control of magnetism toward energy-efficient applications," Appl. Phys. Rev. **8**, 021304 (2021).

[4] A. A. Serga, A. V. Chumak, and B. Hillebrands, "YIG magnonics," J. Phys. D: Appl. Phys. **43**, 264002 (2010).

[5] H. Chiriac, M. Pletea, and E. Hristoforou, "Magneto-surface-acoustic-waves microdevice using thin film technology: Design and fabrication process," Sens. Actuators, A **91**, 107 (2001).

[6] A. Kittmann, P. Durdaut, S. Zabel, J. Reermann, J. Schmalz, B. Spetzler, D. Meyners, N. X. Sun, J. McCord, M. Gerken, G. Schmidt, M. Höft, R. Knöchel, F. Faupel, and E. Quandt, "Wide band low noise love wave magnetic field sensor system," Sci. Rep. **8**, 278 (2018).

[7] C. Kittel, "Interaction of spin waves and ultrasonic waves in ferromagnetic crystals," Phys. Rev. **110**, 836 (1958).

[8] M. F. Lewis and E. Patterson, "Acoustic-surface-wave isolator," Appl. Phys. Lett. **20**, 276 (1972).

[9] R. Sasaki, Y. Nii, Y. Iguchi, and Y. Onose, "Nonreciprocal propagation of surface acoustic wave in Ni/$LiNbO_3$," Phys. Rev. B **95**, 020407(R) (2017).

[10] A. Hernández-Mínguez, F. Macià, J. M. Hernàndez, J. Herfort, and P. V. Santos, "Large nonreciprocal propagation of surface acoustic waves in epitaxial ferromagnetic/semiconductor hybrid structures," Phys. Rev. Appl. **13**, 044018 (2020).

[11] S. Tateno and Y. Nozaki, "Highly nonreciprocal spin waves excited by magnetoelastic coupling in a Ni/Si bilayer," Phys. Rev. Appl. **13**, 034074 (2020).

[12]M. Küß, M. Heigl, L. Flacke, A. Hörner, M. Weiler, M. Albrecht, and A. Wixforth, "Nonreciprocal Dzyaloshinskii–Moriya magnetoacoustic waves," Phys. Rev. Lett. **125**, 217203 (2020).
[13]R. Verba, I. Lisenkov, I. Krivorotov, V. Tiberkevich, and A. Slavin, "Nonreciprocal surface acoustic waves in multilayers with magnetoelastic and interfacial Dzyaloshinskii-Moriya interactions," Phys. Rev. Appl. **9**, 064014 (2018).
[14]R. Verba, V. Tiberkevich, and A. Slavin, "Wide-band nonreciprocity of surface acoustic waves induced by magnetoelastic coupling with a synthetic antiferromagnet," Phys. Rev. Appl. **12**, 054061 (2019).
[15]R. A. Gallardo, T. Schneider, A. K. Chaurasiya, A. Oelschlägel, S. S. P. K. Arekapudi, A. Roldán-Molina, R. Hübner, K. Lenz, A. Barman, J. Fassbender, J. Lindner, O. Hellwig, and P. Landeros, "Reconfigurable spin-wave nonreciprocity induced by dipolar interaction in a coupled ferromagnetic bilayer," Phys. Rev. Appl. **12**, 034012 (2019).
[16]M. Ishibashi, Y. Shiota, T. Li, S. Funada, T. Moriyama, and T. Ono, "Switchable giant nonreciprocal frequency shift of propagating spin waves in synthetic antiferromagnets," Sci. Adv. **6**, eaaz6931 (2020).
[17]M. Krawczyk and D. Grundler, "Review and prospects of magnonic crystals and devices with reprogrammable band structure," J. Phys.: Condens. Matter **26**, 123202 (2014).
[18]M. Jaris, W. Yang, C. Berk, and H. Schmidt, "Towards ultraefficient nanoscale straintronic microwave devices," Phys. Rev. B **101**, 214421 (2020).
[19]P. J. Shah, D. A. Bas, I. Lisenkov, A. Matyushov, N. X. Sun, and M. R. Page, "Giant nonreciprocity of surface acoustic waves enabled by the magnetoelastic interaction," Sci. Adv. **6**, eabc5648 (2020).
[20]M. Küß, M. Heigl, L. Flacke, A. Hörner, M. Weiler, A. Wixforth, and M. Albrecht, "Nonreciprocal magnetoacoustic waves in dipolar-coupled ferromagnetic bilayers," Phys. Rev. Appl. **15**, 034060 (2021).
[21]H. Matsumoto, T. Kawada, M. Ishibashi, M. Kawaguchi, and M. Hayashi, "Large surface acoustic wave nonreciprocity in synthetic antiferromagnets," Appl. Phys. Express **15**, 063003 (2022).
[22]M. Xu, K. Yamamoto, J. Puebla, K. Baumgaertl, B. Rana, K. Miura, H. Takahashi, D. Grundler, S. Maekawa, and Y. Otani, "Nonreciprocal surface acoustic wave propagation via magneto-rotation coupling," Sci. Adv. **6**, eabb1724 (2020).
[23]M. Küß, M. Heigl, L. Flacke, A. Hefele, A. Hörner, M. Weiler, M. Albrecht, and A. Wixforth, "Symmetry of the magnetoelastic interaction of Rayleigh and shear horizontal magnetoacoustic waves in nickel thin films on $LiTaO_3$," Phys. Rev. Appl. **15**, 034046 (2021).
[24]C. K. Campbell, *Surface Acoustic Wave Devices for Mobile and Wireless Communications* (Academic Press, San Diego, 1998).
[25]K. Länge, B. E. Rapp, and M. Rapp, "Surface acoustic wave biosensors: A review," Anal. Bioanal. Chem. **391**, 1509 (2008).
[26]T. Franke, A. R. Abate, D. A. Weitz, and A. Wixforth, "Surface acoustic wave (SAW) directed droplet flow in microfluidics for PDMS devices," Lab Chip **9**, 2625 (2009).
[27]D. P. Morgan, *Surface Acoustic Wave Filters: With Applications to Electronic Communications and Signal Processing*, 2nd ed. (Elsevier, Amsterdam, 2007).
[28]K. Yamanouchi, C. H. S. Lee, K. Yamamoto, T. Meguro, and H. Odagawa, "GHz-range low-loss wide band filter using new floating electrode type unidirectional transducers," in *IEEE 1992 Ultrasonics Symposium. Proceedings* (IEEE, 1992), Vol. 1, pp. 139–142.
[29]R. C. Williamson, "Problems encountered in high-frequency surface-wave devices," in *IEEE 1974 Ultrasonics Symposium. Proceedings* (IEEE, 1974), pp. 321–328.
[30]L. Dreher, M. Weiler, M. Pernpeintner, H. Huebl, R. Gross, M. S. Brandt, and S. T. B. Goennenwein, "Surface acoustic wave driven ferromagnetic resonance in nickel thin films: Theory and experiment," Phys. Rev. B **86**, 134415 (2012).
[31]L. Thevenard, C. Gourdon, J. Y. Prieur, H. J. von Bardeleben, S. Vincent, L. Becerra, L. Largeau, and J.-Y. Duquesne, "Surface-acoustic-wave-driven ferromagnetic resonance in (Ga,Mn)(As,P) epilayers," Phys. Rev. B **90**, 094401 (2014).
[32]M. Huth, F. Porrati, and O. V. Dobrovolskiy, "Focused electron beam induced deposition meets materials science," Microelectron. Eng. **185–186**, 9 (2018).
[33]M. Huth, F. Porrati, and S. Barth, "Living up to its potential – Direct-write nanofabrication with focused electron beams," J. Appl. Phys. **130**, 170901 (2021).
[34]S. A. Bunyaev, B. Budinska, R. Sachser, Q. Wang, K. Levchenko, S. Knauer, A. V. Bondarenko, M. Urbánek, K. Y. Guslienko, A. V. Chumak, M. Huth, G. N. Kakazei, and O. V. Dobrovolskiy, "Engineered magnetization and exchange stiffness in direct-write Co–Fe nanoelements," Appl. Phys. Lett. **118**, 022408 (2021).
[35]O. V. Dobrovolskiy, N. R. Vovk, A. V. Bondarenko, S. A. Bunyaev, S. Lamb-Camarena, N. Zenbaa, R. Sachser, S. Barth, K. Y. Guslienko, A. V. Chumak, M. Huth, and G. N. Kakazei, "Spin-wave eigenmodes in direct-write 3D nanovolcanoes," Appl. Phys. Lett. **118**, 132405 (2021).
[36]M. Krawczyk and H. Puszkarski, "Plane-wave theory of three-dimensional magnonic crystals," Phys. Rev. B **77**, 054437 (2008).
[37]*Three-dimensional Magnonics: Layered, Micro- and Nanostructures*, edited by G. Gubbiotti (Jenny Stanford Publishing, Singapore, 2019).
[38]A. May, M. Hunt, A. van den Berg, A. Hejazi, and S. Ladak, "Realisation of a frustrated 3D magnetic nanowire lattice," Commun. Phys. **2**, 13 (2019).
[39]A. Fernández-Pacheco, L. Skoric, J. M. de Teresa, J. Pablo-Navarro, M. Huth, and O. V. Dobrovolskiy, "Writing 3D nanomagnets using focused electron beams," Materials **13**, 3774 (2020).
[40]Lord Rayleigh, "On waves propagated along the plane surface of an elastic solid," Proc. London Math. Soc. **s1-17**, 4–11 (1885).
[41]M. Weiler, L. Dreher, C. Heeg, H. Huebl, R. Gross, M. S. Brandt, and S. T. B. Goennenwein, "Elastically driven ferromagnetic resonance in nickel thin films," Phys. Rev. Lett. **106**, 117601 (2011).
[42]P. G. Gowtham, T. Moriyama, D. C. Ralph, and R. A. Buhrman, "Traveling surface spin-wave resonance spectroscopy using surface acoustic waves," J. Appl. Phys. **118**, 233910 (2015).
[43]W. P. Robbins, "A simple method of approximating surface acoustic wave power densities," IEEE Trans. Sonics Ultrason. **24**, 339 (1977).
[44]S. Maekawa and M. Tachiki, "Surface acoustic attenuation due to surface spin wave in ferro- and antiferromagnets," AIP Conf. Proc. **29**, 542 (1976).
[45]M. Matsuo, J. Ieda, E. Saitoh, and S. Maekawa, "Effects of mechanical rotation on spin currents," Phys. Rev. Lett. **106**, 076601 (2011).
[46]M. Matsuo, J. Ieda, K. Harii, E. Saitoh, and S. Maekawa, "Mechanical generation of spin current by spin-rotation coupling," Phys. Rev. B **87**, 180402(R) (2013).
[47]D. Kobayashi, T. Yoshikawa, M. Matsuo, R. Iguchi, S. Maekawa, E. Saitoh, and Y. Nozaki, "Spin current generation using a surface acoustic wave generated via spin-rotation coupling," Phys. Rev. Lett. **119**, 077202 (2017).
[48]Y. Kurimune, M. Matsuo, and Y. Nozaki, "Observation of gyromagnetic spin wave resonance in NiFe films," Phys. Rev. Lett. **124**, 217205 (2020).
[49]J.-Y. Duquesne, P. Rovillain, C. Hepburn, M. Eddrief, P. Atkinson, A. Anane, R. Ranchal, and M. Marangolo, "Surface-acoustic-wave induced ferromagnetic resonance in Fe thin films and magnetic field sensing," Phys. Rev. Appl. **12**, 024042 (2019).
[50]Comsol, COMSOL Multiphysics® v. 5.4.Q5: Please provide the Publication Year in Ref. 50.COMSOL AB, Stockholm, Sweden, see www.comsol.com.
[51]D. Cortés-Ortuño and P. Landeros, "Influence of the Dzyaloshinskii–Moriya interaction on the spin-wave spectra of thin films," J. Phys.: Condens. Matter **25**, 156001 (2013).
[52]A. P. van den Heuvel, "Use of rotated electrodes for amplitude weighting in interdigital surface-wave transducers," Appl. Phys. Lett. **21**, 280 (1972).
[53]H. Yatsuda, "Design techniques for SAW filters using slanted finger interdigital transducers," IEEE Trans. Ultrason. Ferroelectr. Freq. Control **44**, 453–459 (1997).
[54]L. Solie, "Tapered transducers-design and applications," in *1998 IEEE Ultrasonics Symposium. Proceedings* (IEEE, 1998), Vol. 1, pp. 27–37.
[55]M. Streibl, F. Beil, A. Wixforth, C. Kadow, and A. C. Gossard, "SAW tomography-spatially resolved charge detection by SAW in semiconductor structures for imaging applications," in *1999 IEEE Ultrasonics Symposium. Proceedings. International Symposium (Cat. No. 99CH37027)* (IEEE, 1999), Vol. 1, p. 11.
[56]L. Keller, M. K. I. Al Mamoori, J. Pieper, C. Gspan, I. Stockem, C. Schröder, S. Barth, R. Winkler, H. Plank, M. Pohlit, J. Müller, and M. Huth, "Direct-write of free-form building blocks for artificial magnetic 3D lattices," Sci. Rep. **8**, 6160 (2018).

[57]F. Porrati, E. Begun, M. Winhold, C. H. Schwalb, R. Sachser, A. S. Frangakis, and M. Huth, "Room temperature $L1_0$ phase transformation in binary CoPt nanostructures prepared by focused-electron-beam-induced deposition," Nanotechnology **23**, 185702 (2012).
[58]M. Hiebel, *Grundlagen der vektoriellen Netzwerkanalyse*, 3rd ed. (Rohde & Schwarz, München, 2011).
[59]The propagation velocity of a Rayleigh-type SAW on a pure Y-cut Z-propagation $LiNbO_3$ substrate with a perfectly conducting overlayer of zero thickness is c_{SAW} = 3404 m/s.[27] We assume that c_{SAW} in the real piezoelectric-ferromagnetic heterostructure is slightly lowered[20] because of mass loading and different elastic constants of $LiNbO_3$ and the magnetic films.
[60]C. Müller, P. Durdaut, R. B. Holländer, A. Kittmann, V. Schell, D. Meyners, M. Höft, E. Quandt, and J. McCord, "Imaging of love waves and their interaction with magnetic domain walls in magnetoelectric magnetic field sensors," Adv. Electron. Mater. **8**, 2200033 (2022).
[61]B. Paschke, A. Wixforth, D. Denysenko, and D. Volkmer, "Fast surface acoustic wave-based sensors to investigate the kinetics of gas uptake in ultra-microporous frameworks," ACS Sens. **2**, 740 (2017).
[62]M. Weiler, A. Brandlmaier, S. Geprägs, M. Althammer, M. Opel, C. Bihler, H. Huebl, M. S. Brandt, R. Gross, and S. T. B. Goennenwein, "Voltage controlled inversion of magnetic anisotropy in a ferromagnetic thin film at room temperature," New J. Phys. **11**, 013021 (2009).
[63]D. Labanowski, A. Jung, and S. Salahuddin, "Power absorption in acoustically driven ferromagnetic resonance," Appl. Phys. Lett. **108**, 022905 (2016).
[64]K. An, A. N. Litvinenko, R. Kohno, A. A. Fuad, V. V. Naletov, L. Vila, U. Ebels, G. de Loubens, H. Hurdequint, N. Beaulieu, J. Ben Youssef, N. Vukadinovic, G. E. W. Bauer, A. N. Slavin, V. S. Tiberkevich, and O. Klein, "Coherent long-range transfer of angular momentum between magnon Kittel modes by phonons," Phys. Rev. B **101**, 060407(R) (2020).
[65]F. Porrati, M. Pohlit, J. Müller, S. Barth, F. Biegger, C. Gspan, H. Plank, and M. Huth, "Direct writing of CoFe alloy nanostructures by focused electron beam induced deposition from a heteronuclear precursor," Nanotechnology **26**, 475701 (2015).
[66]R. Sachser, J. Hütner, C. H. Schwalb, and M. Huth, "Granular Hall sensors for scanning probe microscopy," Nanomaterials **11**, 348 (2021).